Novel optimization methodology for designing unequal-split hybrids toward circulator-free accelerator rf systems

Zhicheng Huang, Yelong Wei,* Yihao Zhang, Chengzhe Wang, Zexin Cao, Li Sun, Zhigang He, Shancai Zhang, and Guangyao Feng

National Synchrotron Radiation Laboratory, University of Science and Technology of China, Hefei, Anhui, China

David Alesini and Luigi Faillace

INFN Frascati National Laboratories, Frascati, Rome, Italy

(Received 19 January 2026; accepted 29 June 2026; published 11 August 2026)

It is significantly challenging to protect the power source against the reflected power when standing-wave rf structures operate, in particular under overcoupled conditions. Conventionally, nonreciprocal circulators, usually operating under pressurized SF_6 atmosphere, are employed to isolate the power source from the reflected power. However, breakdowns, rf losses, and thermal stress make these devices unusable in rf structures operating at high frequencies (6–12 GHz) and can limit the maximum power or the repetition rate, all of which are critical aspects for next-generation accelerators or rf photoinjectors, as an example. Furthermore, the use of SF_6 gas is becoming increasingly problematic due to its environmental impact. In this paper, two novel rf networks are proposed to compensate reflections from standing-wave structures, thus avoiding the use of circulators. They are based on specifically designed hybrids that, combined with rf structures, allow to strongly reduce the reflected power. The design of hybrids with arbitrary power ratios between different ports constitutes a multiobjective optimization problem. To address this challenge, a new optimization methodology is proposed to simplify the optimization process into a single-objective problem. These novel rf networks are then applied to a new C-band photoinjector recently developed at the Italian National Institute of Nuclear Physics INFN (Frascati, Rome, Italy) and to a new proposal of X-band rf photoinjector for National Synchrotron Radiation Laboratory (NSRL).

DOI: 10.1103/b51c-k168

I. INTRODUCTION

In modern accelerator facilities, generating electron beams with high brightness, high repetition rates, and excellent beam quality has become one of the most critical challenges [1,2]. Radiofrequency (rf) photo-guns [3–8] play a central role in producing such beams. They are standing-wave (SW) cavities that intrinsically generate reflected power. Moreover, to meet the demanding requirements of high repetition rate and high cathode peak field, they typically operate with short and high-power (tens of MW) pulses, under overcoupled conditions. This approach reduces the filling time, enabling the delivery of short pulses into the gun. However, operating under an overcoupled condition inherently generates substantial reflected power both during rf transients and in steady-state operation. In conventional rf systems, klystrons or solid-state amplifiers are protected from this reflected power using circulators [9,10].

While circulators have been reliably used in many accelerator facilities, their integration becomes increasingly challenging at high-power, high repetition rates, or high frequencies [11,12] due to increased power losses and rf breakdown phenomena. For example, in high-power (tens of MW), high-repetition-rate (above 100 Hz) C-band (6 GHz) or X-band (12 GHz) systems, circulators are essentially unusable. Furthermore, their size and cost scale unfavorably with increasing peak power and repetition rate, ultimately limiting their applicability and reliability in compact and next-generation accelerator designs, such as colliders [13,14], X-ray free-electron lasers [15], and inverse Compton scattering sources [16–19]. Last but not least, the pressurized SF_6 gas used to prevent discharges in the ferrite is a gas that is expected to be phased out due to its environmental impact. These limitations have motivated significant efforts to reduce, or even eliminate, the reliance on circulators in advanced accelerator systems. For example, a hybrid photoinjector electron source has been proposed to redistribute the reflected power from

*Contact author: wylong@ustc.edu.cn

Published by the American Physical Society under the terms of the Creative Commons Attribution 4.0 International license. Further distribution of this work must maintain attribution to the author(s) and the published article's title, journal citation, and DOI.

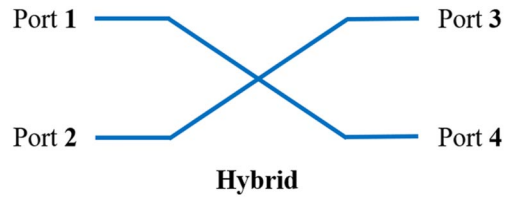


FIG. 1. The schematic of a 4-port hybrid network.

the gun into a coupled traveling-wave (TW) accelerating structure [20]. Such a design can eliminate the requirement for a circulator, with no reflected power transmitted back to the power source. However, in such a system the phase relation between the field of the SW and TW structures is fixed, limiting the possible working points or applications.

In this paper, two topologies based on the specifically designed hybrids are proposed to eliminate the requirement for circulators in such systems. Hybrids are multiport microwave networks [21], which simultaneously achieve low reflection at the input port, high isolation between ports, and, in principle, arbitrary power ratios between ports, as shown in Fig. 1. The scattering matrix of the hybrid in the matched and lossless case is given by

$$S = \begin{bmatrix} s_{11} & s_{12} & s_{13} & s_{14} \\ s_{12} & s_{11} & s_{14} & s_{13} \\ s_{13} & s_{14} & s_{11} & s_{12} \\ s_{14} & s_{13} & s_{12} & s_{11} \end{bmatrix}, \quad (1)$$

where $s_{11} = s_{12} = 0$, $s_{13} = \sqrt{a}e^{j\theta}$, and $s_{14} = \sqrt{b}e^{j(\theta \pm (\pi/2))}$. It should be noted that the phase deviation of $\pm(\pi/2)$ comes from the unitarity of the scattering matrix, not the optimization target.

The design of such devices is a multiobjective optimization problem. Conventional design approaches treat these performance metrics independently, resulting in high computational cost and difficulties in systematically exploring the feasible design space under unitary constraints of the scattering matrix. Grudiev *et al.* proposed a novel methodology for optimizing 4-port 3 dB hybrids and dual-mode polarized couplers [22] by defining a new goal function:

$$\text{Conversion} = |\text{Re}(s_{13})\text{im}(s_{14}) - \text{Re}(s_{14})\text{im}(s_{13})|. \quad (2)$$

This methodology enables a single-objective optimization to simultaneously minimize the reflection and port isolation with equally split power transmitted to two output ports, expressed as $|s_{13}|^2 = |s_{14}|^2 = 0.5$ and a phase deviation between s_{13} and s_{14} of $\pm(\pi/2)$. It has been widely adopted in the optimizations of 3 dB structures, significantly reducing the design complexity. However, for structures with more demanding requirements, such as additional ports and asymmetric power-division ratio, this methodology may become less effective in simplifying the optimizations.

To address these limitations, a novel optimization metric is proposed for the design of arbitrary multiport and arbitrary power ratios between ports, thereby reducing the complexity of the optimization process. This paper is organized as follows. Section II presents the circulator-free topologies for SW cavities using 4-port hybrids. Section III introduces the theoretical basis of the proposed methodology for arbitrary hybrid design with an arbitrary number of ports. In Sec. IV, we apply this methodology to a C-band photoinjector developed at INFN [23,24] and an X-band photoinjector designed for National Synchrotron Radiation Laboratory (NSRL).

II. CIRCULATOR-FREE TOPOLOGY ANALYSIS

To overcome limitations due to the use of a circulator in the feeding of SW structures, three alternative rf topologies based on the use of 4-port hybrids can be adopted. They are schematically represented in Fig. 2, where PC denotes the pulse compressor. Although rf photoinjectors are used as representative examples throughout this paper, the following analysis generally applies to overcoupled SW cavities.

A. The first topology

The first topology shown in Fig. 2(a) has already been adopted for the operation of SW cavities [25]. It allows for near-complete compensation of reflections, while its main disadvantage is that the two cavities are identical. This greatly limits the generalization of the topology to other structures.

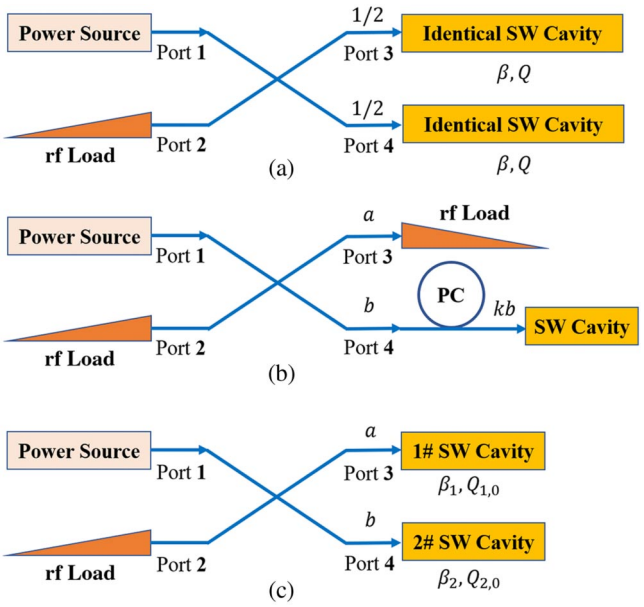


FIG. 2. The circulator-free rf topologies for the SW cavities based on the hybrid networks.

B. The second topology

In the second proposed topology shown in Fig. 2(b), the input power at Port 1 is divided between ports 3 and 4 with a ratio $a:b$, while port 2 remains isolated from port 1. Throughout this paper, the coefficients a and b denote normalized power-division factors of the hybrid, satisfying $a+b=1$. Accordingly, the corresponding wave amplitudes are $\sqrt{a}$ and $\sqrt{b}$. Port 3 can be used to feed an auxiliary structure, typically a TW matched accelerating section with negligible reflections, whereas port 4 drives the main SW cavity. This topology operates effectively when the power delivered to port 4 constitutes only a small fraction of the input power, so that the reflected power is split back by the same factor, strongly reducing the reflected power to the source. To increase the power that feeds the SW cavity, the original long rf pulse can be compressed through a pulse compressor (PC) [26,27]. This scheme has been recently adopted to compensate reflections in a C-band photoinjector [24] system. More precisely, due to the reciprocity, the reflected power from the SW cavity is divided between ports 1 and 2 according to the ratio $b:a$. A fraction a of the input power is absorbed by the load at port 2, while only the remaining fraction b is reflected toward the power source. The reflection coefficient Γ of the SW cavity is correlated to the coupling coefficient β by

$$\Gamma = \left|\frac{\beta-1}{\beta+1}\right|. \tag{3}$$

Then, the steady-state power reflected to the power source can be expressed as

$$P_{\mathrm{ref}} = kP_{\mathrm{in}}b\Gamma^2, \tag{4}$$

where P_{in} is the input power from the power source, and k is the average power amplification factor of the PC. To ensure that the photogun receives the required power after the hybrid and PC and not too much power delivered into the klystron, the feasible ratio should satisfy:

$$\frac{P_{\mathrm{limit}}}{\Gamma^2 P_{\mathrm{cav}}} \geq b \geq \frac{P_{\mathrm{cav}}}{kP_{\mathrm{in,max}}}, \tag{5}$$

where P_{limit} is the maximum allowable reflected power for the klystron, Γ is the reflection coefficient of the SW cavity, and $P_{\mathrm{in,max}}$ is the maximum output power from the klystron. Therefore, Eq. (5) provides a direct design criterion for selecting the hybrid power-division ratio $a:b$ once the maximum allowable reflected power of the rf source and the pulse-compression factor are specified. To analyze the transient process of this topology, with a more precise approach, we can calculate the reflected power from the cavity propagating back to the klystron taking into account its passage through the PC system. The overall transfer function can be expressed as

$$H(\omega) = H_{\mathrm{PC}}(\omega)H_{\mathrm{cav}}(\omega)H_{\mathrm{PC}}(\omega), \tag{6}$$

where $H_{\mathrm{PC}}(\omega)$ and $H_{\mathrm{cav}}(\omega)$ are the transfer function of the PC and SW cavity, defined by [28]:

$$H_{\mathrm{PC}}(\omega) = \frac{\beta_{\mathrm{PC}} - 1 - jQ_{\mathrm{PC},0}\left(\frac{\omega}{\omega_0}-\frac{\omega_0}{\omega}\right)}{\beta_{\mathrm{PC}} + 1 + jQ_{\mathrm{PC},0}\left(\frac{\omega}{\omega_0}-\frac{\omega_0}{\omega}\right)}, \tag{7}$$

$$H_{\mathrm{cav}}(\omega) = \frac{\beta_{\mathrm{cav}} - 1 - jQ_{\mathrm{cav},0}\left(\frac{\omega}{\omega_0}-\frac{\omega_0}{\omega}\right)}{\beta_{\mathrm{cav}} + 1 + jQ_{\mathrm{cav},0}\left(\frac{\omega}{\omega_0}-\frac{\omega_0}{\omega}\right)}, \tag{8}$$

where β_{PC}, β_{cav}, $Q_{\mathrm{PC},0}$, and $Q_{\mathrm{cav},0}$ are the coupling coefficients and unloaded quality factors of PC and SW cavity, ω is the angular frequency of the power source and ω_0 is the resonant angular frequency of the PC and SW cavity. Here, both cavities are assumed to operate at the same frequency. It should be noted that the transfer function $H(\omega)$ of the SW cavities is defined as the ratio of the reflected wave $r(\omega)$ to the incident wave $i(\omega)$, expressed as $H(\omega) = r(\omega)/i(\omega)$, which can be directly derived from the scattering matrices of the components. In this case, it is given by the reflection coefficient of the resonant cavities in Eqs. (7)–(8).

From the physical principle of pulse compression and the above theoretical analysis, the reflected pulse length is typically much shorter than the filling time $\tau_{\mathrm{PC}} = \frac{2Q_{\mathrm{PC},0}}{\omega(1+\beta_{\mathrm{PC}})}$ of the cavity in the pulse compressor. So by the time the pulse ends, very little stored energy remains available for amplification. As a result, the PC introduces almost no power amplification to the reflected power by the cavity. An example is shown in Fig. 3.

This behavior is general and does not depend on a specific rf frequency band. A practical implementation of this scheme, including detailed system parameters and time-domain waveforms for a C-band rf photoinjector, is presented in Sec. IV A.

C. The third topology

In the last topology in Fig. 2(c), the input rf power is injected through port 1 and divided by the hybrid into ports 3 and 4 with a prescribed power ratio $a:b$. Each port feeds a SW structure with an independently designed coupling coefficient but with equal resonant frequency. Port 2 is terminated by a matched load and serves as the isolation port. Owing to the intrinsic properties of the hybrid, the reflected waves from ports 3 and 4 are recombined at ports 1 and 2. If the reflected waves from the two SW cavities have equal amplitudes and opposite phases at port 1, the reflected power at port 1 is canceled, while all reflected power is directed to port 2. In this case, the hybrid exhibits a circulator-like behavior while remaining fully reciprocal

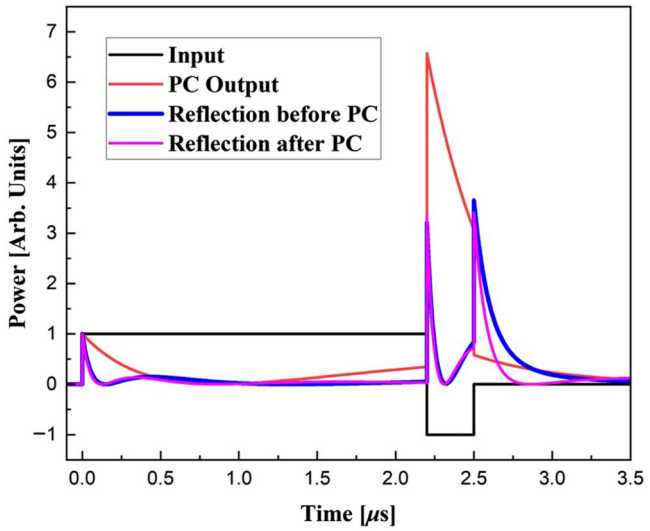


FIG. 3. The transient waveforms of the input power, output power from the PC, the reflected power of an overcoupled cavity before and after PC.

and passive. This topology is similar to the first topology, which has strict requirements: the two cavities must have the same mode, quality factors, and coupling coefficients, and the hybrid must operate with a fixed 1:1 power division. These constraints significantly limit the design flexibility of other SW structures in practical accelerator systems.

In contrast, the present topology relaxes these restrictions by allowing an arbitrary power-division ratio $a:b$ and independently designed coupling coefficients β_3, β_4 for the two SW structures with quality factors $Q_{3,0}$, $Q_{4,0}$. With the input power P_{in}, the out powers at port 3 and 4 are:

$$P_3 = aP_{\text{in}}, \qquad P_4 = bP_{\text{in}}. \tag{9}$$

The reflection coefficient of each cavity, at the resonant frequency of the cavity, is given by

$$\Gamma_i = \left|\frac{\beta_i - 1}{\beta_i + 1}\right|, \qquad i = 3, 4. \tag{10}$$

To achieve cancellation of the reflected power at the input port at steady state, the reflected wave amplitudes from the two cavities must satisfy:

$$aP_3\Gamma_3^2 = bP_4\Gamma_4^2, \tag{11}$$

which establishes a direct relationship between the power-division ratio $a:b$ and the coupling coefficients β_3 and β_4. By substituting Eqs. (9)–(10) into Eq. (11), we can have:

$$\frac{a}{b} = \left|\frac{\beta_3 + 1}{\beta_3 - 1}\right|\left|\frac{\beta_4 - 1}{\beta_4 + 1}\right|. \tag{12}$$

As a result, reflected-power cancellation, at the resonant frequency of the two cavities, can be achieved by appropriately choosing these parameters without requiring identical cavities in terms of unloaded quality factor and coupling coefficient.

Similar to the second topology, the transient processes are also important in terms of both power reflection and filling time. For each SW cavity, the complex field response can be modeled as a single-mode resonator. The electric field inside the cavity evolves as an exponential function [28] with a filling time given by

$$\tau_i = \frac{2Q_{i,0}}{\omega_0(1 + \beta_i)}. \tag{13}$$

To ensure synchronous field build-up in the two SW structures, the two filling times have to be the same, and this gives the condition:

$$\frac{Q_{3,0}}{(1 + \beta_3)} = \frac{Q_{4,0}}{(1 + \beta_4)} = Q_L. \tag{14}$$

Here, Q_L is defined as the loaded quality factor of both cavities. In practice, this expression allows one to calculate, for a given main cavity (characterized by $Q_{3,0}$ and β_3), for which reflections are to be canceled, the coupling coefficient β_4 of a compensating cavity with quality factor $Q_{4,0}$.

The two conditions expressed by Eqs. (12), (14) allow one to simultaneously determine the ideal splitting factor a/b and the coupling coefficient β_4 of the compensating cavity, so as to cancel reflections and obtain the same filling time. The analysis presented above ensures that, under steady-state conditions, the reflected power toward port 1 is ideally canceled by destructive interference at the resonant frequency. However, as already pointed out, for SW structures, the transient reflected power is also important and cannot be neglected.

The transient reflected power can be evaluated considering the frequency-domain reflection coefficient at port 1, which determines the overall reflected response under pulsed excitation. Accordingly, the final reflection coefficient at port 1 can be expressed as

$$s_{11,f} = s_{13}s_{31}R_3 + s_{14}s_{41}R_4, \tag{15}$$

where $s_{13} = \sqrt{a}e^{j\theta}$ and $s_{14} = \pm j\sqrt{b}e^{j\theta}$ and R_3 and R_4 are the reflection coefficients of the two SW cavities given by

$$R_i = \frac{\beta_i - 1 - jQ_{i,0}\left(\frac{\omega}{\omega_0} - \frac{\omega_0}{\omega}\right)}{\beta_i + 1 + jQ_{i,0}\left(\frac{\omega}{\omega_0} - \frac{\omega_0}{\omega}\right)} = \frac{\frac{\beta_i - 1}{\beta_i + 1} - jQ_{i,L}\left(\frac{\omega}{\omega_0} - \frac{\omega_0}{\omega}\right)}{1 + jQ_{i,L}\left(\frac{\omega}{\omega_0} - \frac{\omega_0}{\omega}\right)}, \qquad i = 3, 4. \tag{16}$$

According to Eq. (14), $Q_{3,L}$ and $Q_{4,L}$ are equal to Q_L. It should be noted that the reflection coefficient s_{11}, s_{33}, s_{44} is zero when the hybrid is matched. By designing the phase deviation between s_{13} and s_{14} (correctly designing the waveguide length in order to have $arg(s_{13}/s_{14}) = \pm(\pi/2)$), the minimum value of $s_{11,f}$ can be obtained combining Eqs. (12)–(16) and it is given by

$$\begin{aligned} s_{11,f} &= (aR_3 - bR_4)e^{2j\theta} \\ &= \frac{a\frac{\beta_3-1}{\beta_3+1} - b\frac{\beta_4-1}{\beta_4+1} - j(a-b)Q_L(\frac{\omega}{\omega_0} - \frac{\omega_0}{\omega})}{1 + jQ_L(\frac{\omega}{\omega_0} - \frac{\omega_0}{\omega})} e^{2j\theta} \\ &= \frac{-j(a-b)Q_L(\frac{\omega}{\omega_0} - \frac{\omega_0}{\omega})}{1 + jQ_L(\frac{\omega}{\omega_0} - \frac{\omega_0}{\omega})} e^{2j\theta}. \end{aligned} \tag{17}$$

Here, it is assumed that the resonant frequencies of both SW structures are the same. It can be found that at the resonant frequency, it has a perfect cancellation on the steady-state reflected power similar to the critical-coupling cavity. For the critical-coupling cavity with the same unloaded quality factor $Q_{3,0}$ and a coupling coefficient of $\beta_3 = 1$, the reflection coefficient corresponding to Eq. (16) is expressed by

$$R_3 = \frac{-j\frac{Q_{3,0}}{2}(\frac{\omega}{\omega_0} - \frac{\omega_0}{\omega})}{1 + j\frac{Q_{3,0}}{2}(\frac{\omega}{\omega_0} - \frac{\omega_0}{\omega})}. \tag{18}$$

Compared with the critical-coupling cavity, a suppression ratio of $|a-b|$ is introduced into the transient reflected power at port 1 according to Eq. (17). Due to the fact that $|a-b| < 1$, the final reflection coefficient spectrum $s_{11,f}$ is much lower than the critical-coupling cavity, greatly reducing the transient reflected power. Additionally, $Q_L < Q_{3,0}$ holds at the overcoupled condition, further expanding the bandwidth and suppressing the transient reflected power.

To design the such an rf system, the filling time of the main cavity is first determined in order to optimize the efficiency of the input power for a given rf pulse width t_p. For SW cavities operating under overcoupled conditions, a practical choice is to select the filling time in the range of approximately $t_p/3$ to $t_p/2.3$, such that the transient field response reaches about 90% of its steady-state value within the rf pulse.

Once the filling time is fixed, the required coupling coefficients β_3 can be calculated using Eq. (13). Taking into account different unloaded quality factors $Q_{3,0}$, $Q_{4,0}$ of the main cavity and the compensating cavity, β_4 of the compensating cavity is determined by Eq. (14). Based on the obtained values of β_3 and β_4, the corresponding power ratio $a:b$ of the hybrid can then be determined from Eq. (12). An X-band implementation for NSRL is taken as an example, presented in Sec. IV B.

However, realizing such a hybrid in both topologies requires enforcing multiple S-parameter constraints of the hybrid simultaneously, which inherently leads to a multiobjective problem. These challenges motivate the development of a new single-objective metric, presented in Sec. III.

III. NEW METHODOLOGY FOR HYBRID DESIGN

In the circulator-free topology proposed in the previous section, the most critical device is the 4-port unequal-split hybrid. The design is a multiobjective optimization process, expressed by

$$|s_{11}| = 0, \quad |s_{12}| = 0, \quad |s_{13}| : |s_{14}| = a : b. \tag{19}$$

Here, a and b satisfy $a + b = 1$. Such a multiparameter and multiobjective problem is too complicated for the optimizations in the simulations. To solve this issue, a novel metric is proposed to be a single-objective power-ratio function to simplify this problem, expressed as

$$G = \sqrt{a^a b^b} - |s_{13}|^a |s_{14}|^b. \tag{20}$$

Minimizing G is equivalent to forcing $|s_{13}|^a|s_{14}|^b$ to reach its theoretical maximum. Then, we can prove that the maximum value is achieved if and only if the target in Eq. (19) is satisfied. It should be noted that all the following and simulations are under the physical constraints of a lossless and reciprocal 4-port network.

For a lossless and reciprocal 4-port network, we have:

$$|s_{11}|^2 + |s_{12}|^2 + |s_{13}|^2 + |s_{14}|^2 = 1, \tag{21}$$

which represents the conservation of energy in the network. Then, we define a parameter $K = 1 - |s_{11}|^2 - |s_{12}|^2$, and then, we get the constraint:

$$|s_{13}|^2 + |s_{14}|^2 = K. \tag{22}$$

For simplicity, we let $x := |s_{13}|, y := |s_{14}|$. In order to obtain the maximum of $x^a y^b$, we define the Lagrangian function using the constraint Eq. (22):

$$L(x, y, \lambda) = x^a y^b - \lambda(x^2 + y^2 - K), \tag{23}$$

where λ is the Lagrangian constant. Setting the partial derivatives to zero yields:

$$\frac{\partial L}{\partial x} = ax^{a-1}y^b - 2\lambda x = 0, \tag{24}$$

$$\frac{\partial L}{\partial y} = bx^a y^{b-1} - 2\lambda y = 0, \tag{25}$$

$$\frac{\partial L}{\partial \lambda} = x^2 + y^2 - K = 0. \tag{26}$$

Combining Eqs. (24)–(25), we have:

$$\frac{x^2}{y^2} = \frac{a}{b}. \tag{27}$$

Applying the constraint Eq. (26), x and y can be calculated:

$$x = \sqrt{Ka}, \qquad y = \sqrt{Kb}, \tag{28}$$

which corresponds exactly to the desired power ratio. And s_{11} and s_{12} converge at 0 with K approaching to 1. Then, we can calculate the maximum value of $|s_{13}|^a|s_{14}|^b$:

$$(|s_{13}|^a|s_{14}|^b)_{\max} = \sqrt{a^a b^b}. \tag{29}$$

Since the value of $|s_{13}|^a|s_{14}|^b$ is bounded, and the feasible set is compact, the above solution is the unique feasible maximum. Correspondingly, the metric reaches zero if and only if Eq. (19) is satisfied. This demonstrates that driving this metric to zero automatically enforces the required power ratio and matching of the full hybrid design. Mathematically, this proves uniqueness. Physically, it reflects that a lossless hybrid has only one feasible S-matrix satisfying the prescribed power ratio and matching conditions. This metric remains convex-like in practice, which means that the optimum is the global optimum, enabling a stable optimization process. By using it in the optimizations of hybrid, it can guide the simulations well and greatly simplify the full design.

In addition, this new metric can be extended to the structures with an arbitrary number of ports and prescribed power ratios. For a network with n ports to extract power with the prescribed power ratio of $a_1 : a_2 : \cdots : a_n$, while m ports are isolated with the input port:

$$|s_{1i}| = 0, \qquad i = 1, 2, \ldots, m+1, \tag{30}$$

$$\begin{aligned} &|s_{1,i+m+1}| : |s_{1,i+m+2}| : \cdots : |s_{1,i+m+n}| \\ &= a_1 : a_2 : \cdots : a_n, \qquad i = 1, 2, \ldots, n, \end{aligned} \tag{31}$$

$$\sum_{i=1}^{n} a_i = 1. \tag{32}$$

Such a network with $(n+m+1)$ ports is very complicated if considering multiobjective optimizations. To make it possible to optimize this network, Eq. (20) can be redefined as

$$G = \sqrt{\prod_{i=1}^{n} a_i^{a^i}} - \prod_{i=1}^{n} |s_{1,m+1+i}|^{a_i}, \tag{33}$$

while the constraint for the lossless and reciprocal network is

$$\sum_{i=1}^{n} |s_{1,m+1+i}|^2 = 1 - \sum_{i=1}^{m+1} |s_{1,i}|^2 = K. \tag{34}$$

For simplicity, we let $x_i := |s_{1,m+1+i}|$ $(i = 1, 2, \ldots, n)$. The Lagrangian function can be defined as

$$L(x_{1,2,\ldots,i,\ldots,n}, \lambda) = \prod_{i=1}^{n} x_i^{a_i} - \lambda\left(\sum_{i=1}^{n} x_i^2 - K\right). \tag{35}$$

Setting the partial derivatives to zero yields for every x_i and λ:

$$\frac{\partial L}{\partial x_i} = \frac{a_i \prod_{j=1}^{n} x_j^{a_j}}{x_i} - 2\lambda x_i = 0, \quad i = 1, 2, \ldots, n, \tag{36}$$

$$\frac{\partial L}{\partial \lambda} = \sum_{i=1}^{n} x_i^2 - K = 0. \tag{37}$$

By rearranging Eq. (36), we can have:

$$\frac{a_1}{x_1^2} = \frac{a_2}{x_2^2} = \cdots = \frac{a_i}{x_i^2} = \cdots = \frac{a_n}{x_n^2}, \tag{38}$$

which corresponds to the prescribed power ratio. Applying the constraint Eq. (37), x_i can be calculated:

$$x_i = \sqrt{Ka_i}, \tag{39}$$

which corresponds exactly to the desired power ratio. And similar to that in the previous 4-port network, the matching of the structure is satisfied with K approaching to 1. The maximum value can be obtained:

$$\left(\prod_{i=1}^{n} |s_{1,m+1+i}|^{a_i}\right)_{\max} = \sqrt{\prod_{i=1}^{n} a_i^{a_i}}. \tag{40}$$

G has the unique global minimum if and only if Eqs. (30)–(31) are satisfied. This generalization enables systematic design of complex multiport power-distribution networks, which were previously impractical due to the high dimensionality of the multiobjective space.

IV. EXAMPLES OF THE DESIGN OF CIRCULATOR-FREE SYSTEMS

This section focuses on the practical validation of the proposed circulator-free topologies through full-wave simulations and experimental results. Representative C-band and X-band implementations are discussed to demonstrate the applicability of the proposed design methodology. First, a 9:1 asymmetric hybrid is combined with the C-band photoinjector developed at INFN to evaluate the performance of the second topology. This scheme has been successfully adopted for the high-power test performed at PSI [24]. The second example is related to the third topology, and we will illustrate a 3:2 hybrid design combined with an X-band photoinjector and a 3-cell SW compensating structure designed for NSRL.

A. C-band hybrid structure design and experiments

The asymmetric hybrid in this study is an H-type four-port structure operating at 5.712 GHz, as shown in Fig. 4(a). The 4 ports are implemented using the WR187 (standard waveguides, featuring dimensions of 47.55 mm × 22.15 mm). rf power is fed from port 1 and distributed into port 3 and port 4 with a 9:1 power ratio, while port 2 is isolated from port 1. Due to the symmetry of the four ports, the scattering matrix must satisfy a set of unitarity and reciprocity constraints as illustrated in Sec. III. The C-band photoinjector model is shown in Fig. 4(b), and the corresponding rf parameters are summarized in Table I. As already pointed out, they are referred to the C-band photoinjector developed at INFN [24]. All simulations in this section have been conducted using HFSS and CST Microwave Suite [29,30].

The required input rf power of the photogun cavity is $P_{\mathrm{cav}} = 20$ MW, while the available power from the klystron is $P_{\mathrm{in}} = 45$ MW. The amplification factor of the pulse compressor with a 2.5 us klystron pulse and a 300 ns rf pulse (required for the filling of the gun) is $k = 4.5$. We have also considered a P_{limit} of $(1\% \sim 2\%)P_{\mathrm{in}}$. Based on these parameters and according to Eq. (5), b should satisfy $0.18 \geq b \geq 0.1$. In particular, with $b = 0.1$ (the current choice of [24]) using Eq. (4), the average power reflected into the klystron (at regime) is calculated to be $P_{\mathrm{ref}} = 500$ kW, which is below the maximum allowable reflected power for the klystron in the power source system. To optimize the hybrid, the metric G in Eq. (20) is employed in the optimization process to simplify the design. The results of the electromagnetic simulations of the hybrid are presented in Fig. 5, where all the scattering parameters are given in the frequency range 5.712 ± 50 MHz. In the same plot, we have also reported the amplitudes of the electromagnetic field with 45 MW input power. The S parameters exhibit a 20 dB bandwidth in the range ±30 MHz centered at 5.712 GHz, with $20\log|s_{11}|$ and $20\log|s_{12}|$ below −40 dB and $20\log|G|$ below −80 dB at the operating frequency. The power ratio between port 3 and Port 4 is 9:1 at 5.712 GHz. The peak surface electric and magnetic fields are approximately 26 MV/m and 80 kA/m.

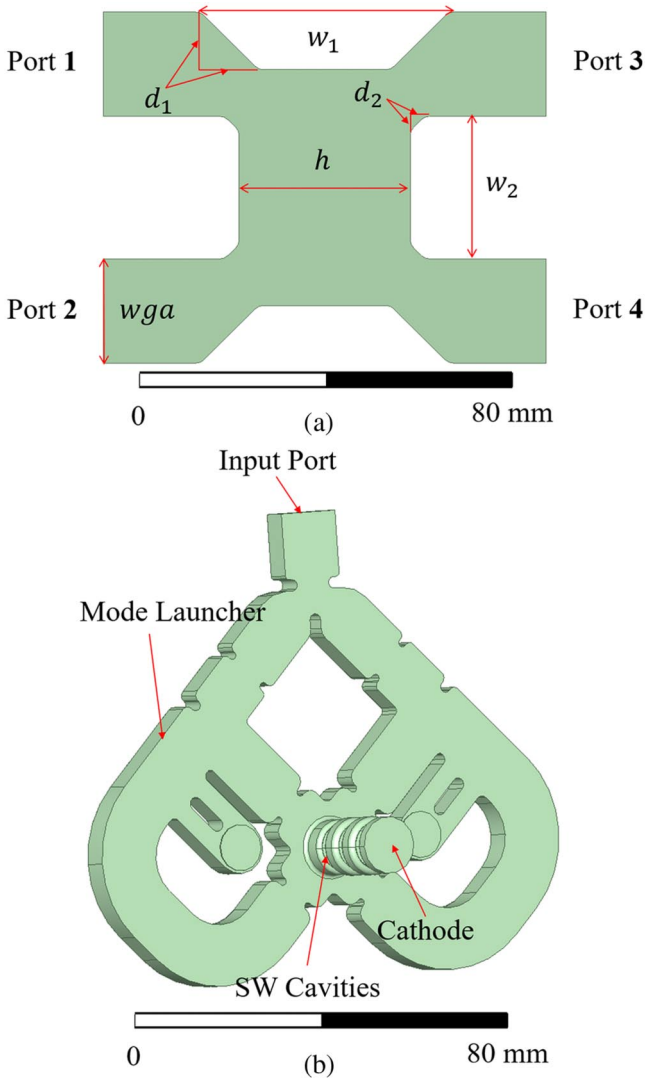


FIG. 4. Geometry models of (a) the 4-port H-type hybrid and (b) the C-band photoinjector used in the following simulations.

TABLE I. Parameters of the C-band photogun.

Parameters	Value	Unit
Operating frequency f	5.712	GHz
Required rf input power	20	MW
Repetition rate	400	Hz
Cathode peak field	160	MV/m
Shunt impedance R_s	3.48	MΩ
Quality factor Q	11900	
Coupling coefficient β	3	
Filling time τ	138	ns
rf pulse length t_p	300	ns

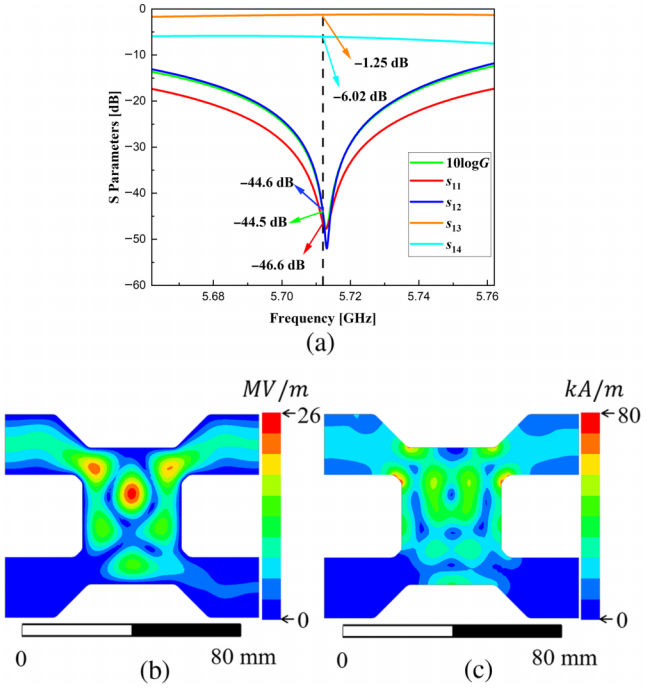


FIG. 5. The S parameters (a), electric (b) and magnetic (c) fields of the C-band 9:1 hybrid.

The amplitudes of the rf input and reflected pulses have been then calculated and are shown in Fig. 6. We have considered a nominal input power $P_{\text{in}} = 45$ MW. Figure 6(a) shows the real case of a rise and fall time of the rf pulse and a phase transition time of 10 ns. Just for comparison, we have reported in Fig. 6(b) the case of step-like rf transitions. It can be noted that, with this proposed scheme, the reflected power to port 1 exhibits three small and very short peaks with a maximum peak power of $P_{\text{ref,peak}} = 1.2$ MW. It is worth noting that even under extreme conditions such as rf breakdown in the cavity, which may lead to nearly total reflection ($|\Gamma| \approx 1$), the power reflected to the klystron remains strongly suppressed by the hybrid. According to Eq. (4), only a fraction b of the reflected power is directed back to Port 1. For the present design with $b = 0.1$, this corresponds to a reflected power on the order of approximately 2 MW. This is well within the tolerance of klystron operation for occasional breakdown events or conditioning processes, indicating a robust behavior of the proposed scheme under nonideal operating conditions. These calculations are in quite good agreement with the experimental results found during the high-power rf test of the C-band gun [24].

B. X-band hybrid structure design

In order to validate the third topology introduced in Sec. II, an X-band implementation operating at

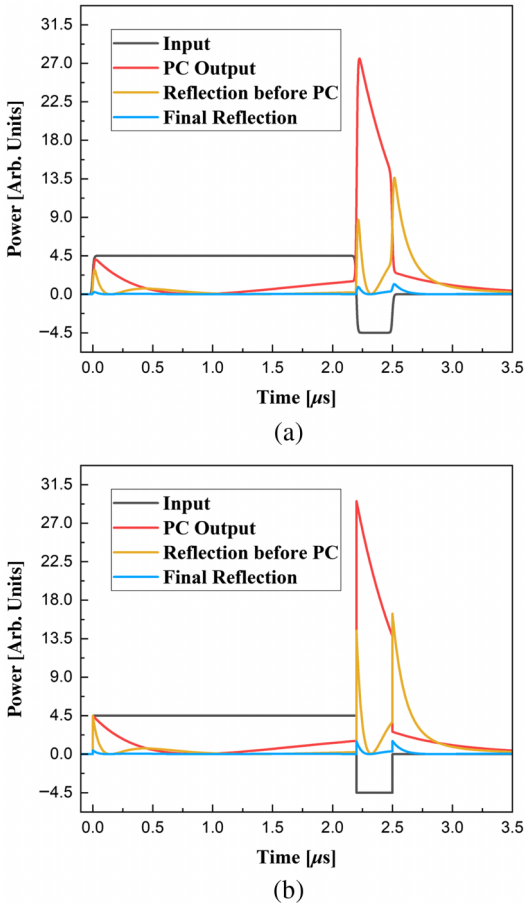


FIG. 6. The transient waveforms of the input power, output power from the PC, the reflected power of the injector before PC and final reflected power into the power source with (a) and without (b) a transition time of 10 ns.

11.424 GHz has been developed for the NSRL photoinjector system. The configuration consists of a 4-port hybrid, a normal-conducting X-band 2.3-cell photogun, and an additional 3-cell SW structure, as illustrated in Fig. 7.

The system is designed to operate with an rf pulse length of $t_p = 200$ ns. To ensure consistent transient behavior of the two SW structures, a filling time of $\tau = 67$ ns (approximately $t_p/3$) is selected. From eigenmode simulations, the unloaded quality factors are obtained as $Q_{3,0} = 7250$ for the photogun and $Q_{4,0} = 8970$ for the 3-cell cavity. Using Eq. (13), the coupling coefficient of the photogun is calculated as $\beta_3 = 1.86$. The coupling coefficient of the compensating cavity is then determined from Eq. (14) to enforce an identical transient process, corresponding to $\beta_4 = 2.64$.

Based on these coupling coefficients, the required power-division ratio of the hybrid is derived from Eq. (12), resulting in $a = 0.6$ and $b = 0.4$, corresponding to a 3:2 power ratio between the two output ports.

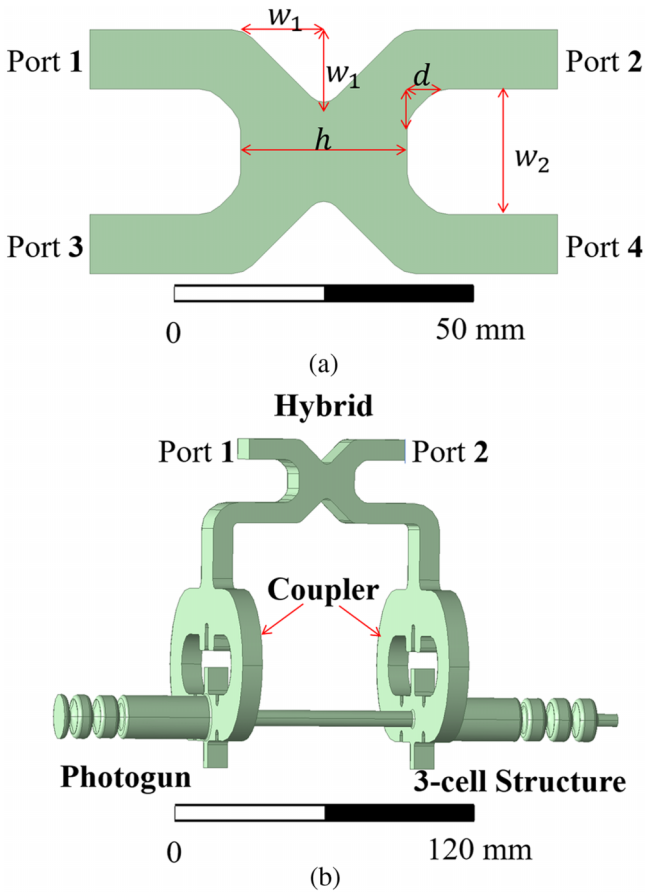


FIG. 7. Geometry models of (a) the 4-port E-type hybrid and (b) the X-band photoinjector used in the following simulations.

The main rf parameters of the full structure are summarized in Table II. The required rf input power of the photogun is 6 MW in order to achieve a cathode peak field of 200 MV/m, while the compensating structure requires 4 MW. Therefore, the total input power at port 1 of the hybrid is approximately 10 MW.

TABLE II. Parameters of both X-band structures and the full structure.

Parameters	Photogun	3-cell structure	Unit
Operating frequency f	11.424	11.424	GHz
Required rf input power	6	4	MW
Repetition rate	400	400	Hz
Cathode peak field	200		MV/m
Shunt impedance R_s	2.00	3.55	MΩ
Quality factor Q	7250	8970	
Coupling coefficient β	1.86	2.64	
Reflected power P_{ref}	906	1360	kW
Filling time τ	67	67	ns
rf pulse length t_p	200	200	ns
Peak reflected power		400	kW
Average reflected power		< 100	kW

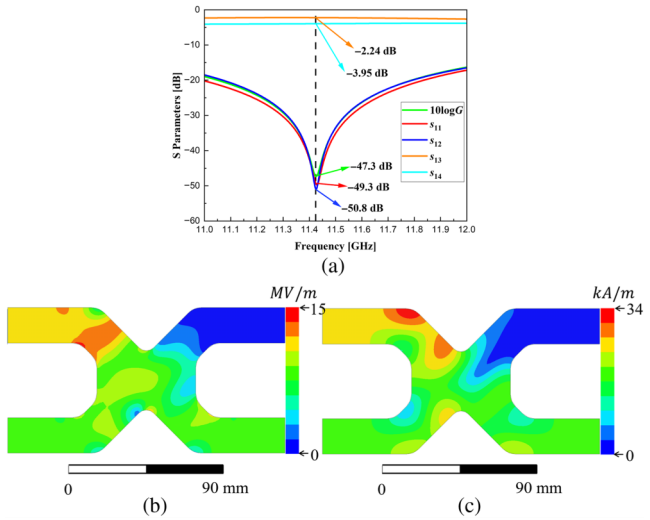
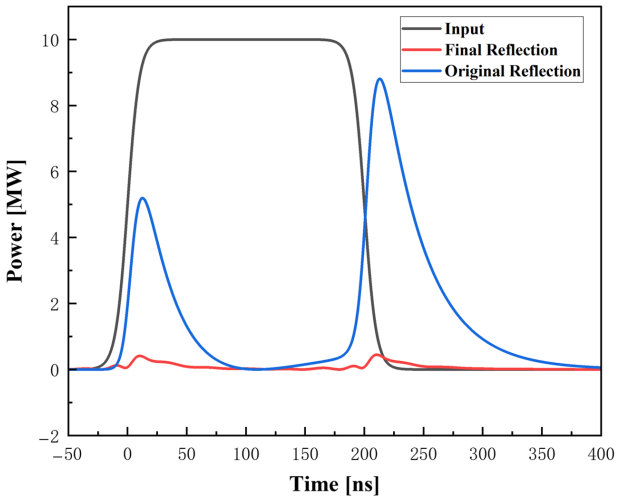


FIG. 8. The S parameters (a), electric (b), and magnetic (c) fields of the X-band 3:2 hybrid.

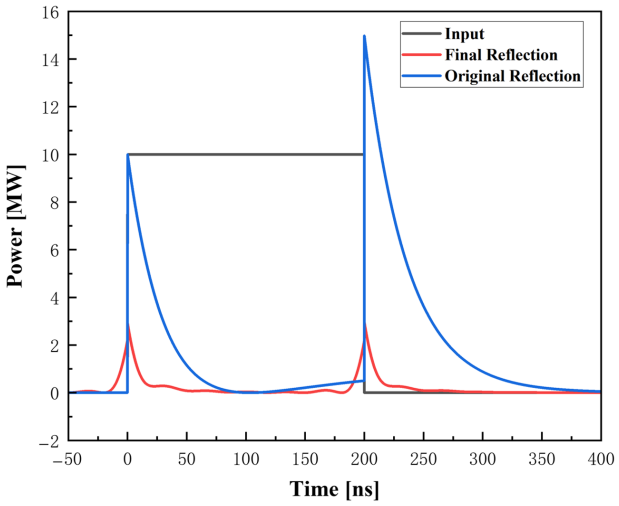
The results of the electromagnetic simulations of the hybrid are presented in Fig. 8. The amplitudes of the electromagnetic fields with 10 MW input power. At the operating frequency, $20\log|S_{11}|$ and $20\log|S_{12}|$ are below −40 dB, while the power ratio between the two output ports closely matches 3:2. The value of $20\log|G|$ is below −80 dB at 11.424 GHz, indicating proper convergence of the optimization process.

To evaluate the performance of the complete system under pulsed conditions, the amplitudes of the rf input and reflected pulses have been calculated and are shown in Fig. 9 with a nominal input power of $P_{\mathrm{in}} = 10$ MW. Figure 9(a) includes a realistic rise and fall time of 10 ns, while Fig. 9(b) shows the idealized case with step-like transitions for comparison.

It can be observed that the reflected power at port 1 remains significantly suppressed over the entire rf pulse compared with the original reflection from the photogun. In Fig 9(a), the peak reflected power is approximately 400 kW, while the average reflected power remains below 100 kW. This analysis confirms the elimination of the reflected waves from the two SW structures in this topology while offering significantly greater design flexibility than the conventional hybrid structures, thereby validating the effectiveness of the proposed hybrid-based circulator-free topology. Even in the presence of rf breakdown in one of the cavities, the system remains inherently robust. Considering a worst case where a breakdown in the photogun leads to nearly total reflection ($|R_3| \approx 1$), the power reflected to the rf source is still significantly reduced due to the reciprocity of the hybrid network. In this case, only a fraction of the reflected power is directed back to port 1, while the remaining part is terminated by the rf load at port 2. For the present design, the maximum reflected power reaching the klystron is estimated to be approximately 3.6 MW, and the corresponding pulse



(a)



(b)

FIG. 9. The transient waveforms of the input power, the output power at port 1 for the second topology and original reflected power from the SW cavity at port 3 with (a) and without (b) a transition time of 10 ns.

length is very short compared with the rf pulse length. This is generally tolerable for klystron operation and are not expected to cause too much damage.

The simulated S-parameters and logarithmic-scale field distributions of the integrated system are shown in Fig. 10. The input reflection coefficient $20\log|S_{11}|$ remains below −20 dB over a reasonable bandwidth, while nearly all reflected power is directed to port 2. And the electromagnetic fields of the compensating cavity are slightly lower than those in the photogun, enabling better high-power performance on breakdowns. These results clearly verify the effectiveness of the second hybrid-based topology proposed in Sec. II and demonstrate its applicability to X-band accelerator systems.

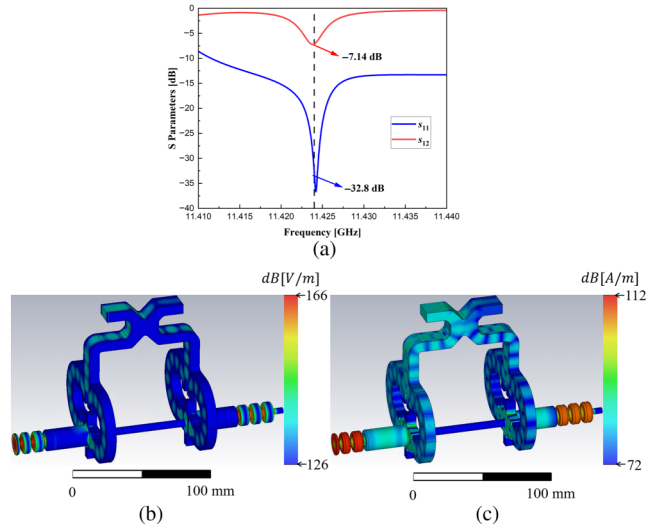


FIG. 10. The S parameters (a), logarithmic-scale electric (b), and magnetic (c) fields of the combined structure with hybrid, photogun and 3-cell structure.

V. CONCLUSIONS

In this paper, three circulator-free rf topologies based on unequal-split multiport hybrids have been proposed for mitigating reflected power in SW structures, aiming to remove the dependence on high-power circulators while ensuring stable operation under high-gradient and high-repetition-rate conditions.

To enable the practical implementation of these configurations, a novel optimization metric has been introduced for the design of unequal-split multiport hybrids. The proposed metric converts the inherently multiobjective problem—simultaneously involving input matching, port isolation, and prescribed power-division ratios—into a single-objective formulation. Due to its general definition, the metric can be extended to an arbitrary number of ports and arbitrary power-splitting ratios, providing a systematic and efficient design approach for complex rf networks. The first topology has already been adopted in previous implementations [25] and is based on the use of a 3-dB hybrid coupler. The power is equally distributed between two identical cavities, and the reflected power is recombined by the hybrid and dissipated at the fourth port of the device. To overcome the limitations of the first topology associated with the use of two identical cavities, two alternative topologies have been proposed. The first topology is based on the use of a 4-port hybrid and a pulse compressor. By properly selecting the power-division ratio, the hybrid redistributes the reflected power between the isolation port and the rf source, while the pulse compressor amplifies only the forward power delivered to the cavity. A C-band implementation based on a 9:1 H-type hybrid has been designed and experimentally validated [24]. Both electromagnetic

simulations and high-power tests confirm that the reflected power toward the rf source remains within acceptable operational limits.

The second topology employs a hybrid to simultaneously feed two SW structures. By selecting the power-division ratio and the coupling coefficients of both cavities, the reflected waves from both structures are destructively recombined at the input port, while the remaining reflected power is directed to the isolation port. An X-band implementation has been developed to illustrate this concept. Time-domain and frequency-domain simulations demonstrate that the reflected power toward the rf source remains negligible under both steady-state and transient operating conditions.

Overall, the proposed hybrid-based rf topologies provide a practical and scalable alternative to conventional circulator-based systems for high-power accelerator applications.

ACKNOWLEDGMENTS

This work is supported by the National Key Research and Development Program of China (No. 2024YFA1612200), the "Hundred Talents Program" of the Chinese Academy of Sciences (No. KJ2310007003), the Fundamental Research Funds for the Central Universities (No. WK2310000114), and Chinese Academy of Sciences President's International Fellowship Initiative (No. 2025PD0102).

DATA AVAILABILITY

The data that support the findings of this article are not publicly available upon publication because it is not technically feasible and/or the cost of preparing, depositing, and hosting the data would be prohibitive within the terms of this research project. The data are available from the authors upon reasonable request.

[1] L. Rigon, X-ray imaging with coherent sources, Compr. Biomed. Phys. **2**, 193 (2014).

[2] D. Angal-Kalinin *et al.*, Design, specifications, and first beam measurements of the compact linear accelerator for research and applications front end, Phys. Rev. Accel. Beams **23**, 044801 (2020).

[3] R. R. Robles *et al.*, Versatile, high brightness, cryogenic photoinjector electron source, Phys. Rev. Accel. Beams **24**, 063401 (2021).

[4] B. E. Carlsten, New photoelectric injector design for the Los Alamos National Laboratory XUV FEL accelerator, Nucl. Instrum. Methods Phys. Res., Sect. A **285**, 313 (1989).

[5] F. Zhou *et al.*, Commissioning of the SLAC linac coherent light source ii electron source, Phys. Rev. Accel. Beams **24**, 073401 (2021).

[6] T. G. Lucas *et al.*, Toward a brightness upgrade to the SwissFEL: A high gradient traveling-wave rf photogun, Phys. Rev. Accel. Beams **26**, 103401 (2023).

[7] M. Schaer, A. Citterio, P. Craievich, S. Reiche, L. Stingelin, and R. Zennaro, Rf traveling-wave electron gun for photoinjectors, Phys. Rev. Accel. Beams **19**, 072001 (2016).

[8] J.-X. Wang, K. Zhou, P. Li, D.-X. Xiao, L.-J. Shan, X.-M. Shen, Y. Liu, Z. Zhou, H.-B. Wang, and D. Wu, High-brightness photo-injector with standing-wave buncher-based ballistic bunching scheme for inverse compton scattering light source, Nucl. Sci. Tech. **33**, 44 (2022).

[9] C. Weil, Overview of high power ferrite devices and key considerations for the design, operation and high-power testing of ferrite circulators, in *Proceedings of 12th CW and High Average Power RF Workshop* (JACoW Publishing, Geneva, Switzerland, 2022).

[10] C. Mi, C. Zhao, Z. Liu, T. Luo, C. Huang, D. K. Agrawal, Y. Zhang, and K. Huang, Compact four-port waveguide circulator using discrete ferrites for injection-locking magnetron system, Electronics **13**, 997 (2024).

[11] Y. M. Jain, P. K. Sharma, K. Ambulkar, P. R. Parmar, A. R. Jadhav, and H. V. Dixit, Steady-state operation of high cw power circulator: Challenges and solutions through simulation and experiments, IEEE Trans. Plasma Sci. **48**, 1290 (2020).

[12] E. Schlomann, J. Green, and J. Saunders, Ultimate performance limitations of high-power ferrite circulators and phase shifters, IEEE Trans. Magn. **1**, 168 (1965).

[13] V. Shiltsev and F. Zimmermann, Modern and future colliders, Rev. Mod. Phys. **93**, 015006 (2021).

[14] L. Schoeffel, C. Baldenegro, H. Hamdaoui, S. Hassani, C. Royon, and M. Saimpert, Photon-photon physics at the LHC and laser beam experiments, present and future, Prog. Part. Nucl. Phys. **120**, 103889 (2021).

[15] J. B. Rosenzweig *et al.*, An ultra-compact x-ray free-electron laser, New J. Phys. **22**, 093067 (2020).

[16] P. Niknejadi, J. M. D. Kowalczyk, M. R. Hadmack, B. T. Jacobson, I. Howe, S. Kan, S. Smith, E. B. Szarmes, G. Varner, and J. M. J. Madey, Free-electron laser inverse-compton interaction x-ray source, Phys. Rev. Accel. Beams **22**, 040704 (2019).

[17] R. W. Schoenlein, W. P. Leemans, A. H. Chin, P. Volfbeyn, T. E. Glover, P. Balling, M. Zolotorev, K.-J. Kim, S. Chattopadhyay, and C. V. Shank, Femtosecond x-ray pulses at 0.4 Å generated by 90° Thomson scattering, Science **274**, 236 (1996).

[18] C. Tang *et al.*, Tsinghua Thomson scattering x-ray source, Nucl. Instrum. Methods Phys. Res., Sect. A **608**, S70 (2009).

[19] K. Dupraz *et al.*, The ThomX ICS source, Phys. Open **5**, 100051 (2020).

[20] L. Faillace *et al.*, High field hybrid photoinjector electron source for advanced light source applications, Phys. Rev. Accel. Beams **25**, 063401 (2022).

[21] C. D. Nantista *et al.*, Planar waveguide hybrids for very high power rf, in *Proc. Particle Accelerator Conf.* (IEEE, New York, 1999), p. 1432.

[22] A. Grudiev, Design of compact high power rf components at x-band, CLIC Note 1067, 2016.
[23] A. Giribono *et al.*, Dynamics studies of high brightness electron beams in a normal conducting, high repetition rate C-band injector, Phys. Rev. Accel. Beams **26**, 083402 (2023).
[24] D. Alesini *et al.*, Design, realization, and testing of a brazing-free C-band radio frequency photogun, Phys. Rev. Accel. Beams **29**, 012001 (2026).
[25] D. Alesini and F. Marcellini, Rf deflector design of the CLIC test facility CTF3 delay loop and beam loading effect analysis, Phys. Rev. ST Accel. Beams **12**, 031301 (2009).
[26] Z. Farkas, SLED: A method of doubling SLAC's energy, in *Proc. Int. Conf. High Energy Accelerators* (U.S. Atomic Energy Commission, Washington, DC, USA, 1974), p. 576.
[27] X. Lin *et al.*, Two-stage rf pulse compression system with correction cavity chain, Phys. Rev. Accel. Beams **25**, 120401 (2022).
[28] T. P. Wangler, *RF Linear Accelerators* (John Wiley & Sons, Hoboken, NJ, 2008).
[29] ANSYS HFSS, ANSYS, Inc., Canonsburg, PA, USA.
[30] CST Studio Suite, Dassault Systèmes SIMULIA, Vélizy-Villacoublay, France.